Supplementary materials for the article

Mineralogy and crystal chemistry of Mn, Fe, Co, Ni, and Cu in a deep-sea Pacific polymetallic nodule

ALAIN MANCEAU[1,*] MARTINE LANSON[1] AND YOSHIO TAKAHASHI[2]

[1]ISTerre, Univ. Grenoble Alpes and CNRS, F-38041 Grenoble, France.

[2]Institute for Sustainable Sciences and Development, Hiroshima University, 1-3-1 Kagamiyama, Higashi-Hiroshima 739-8526, Japan

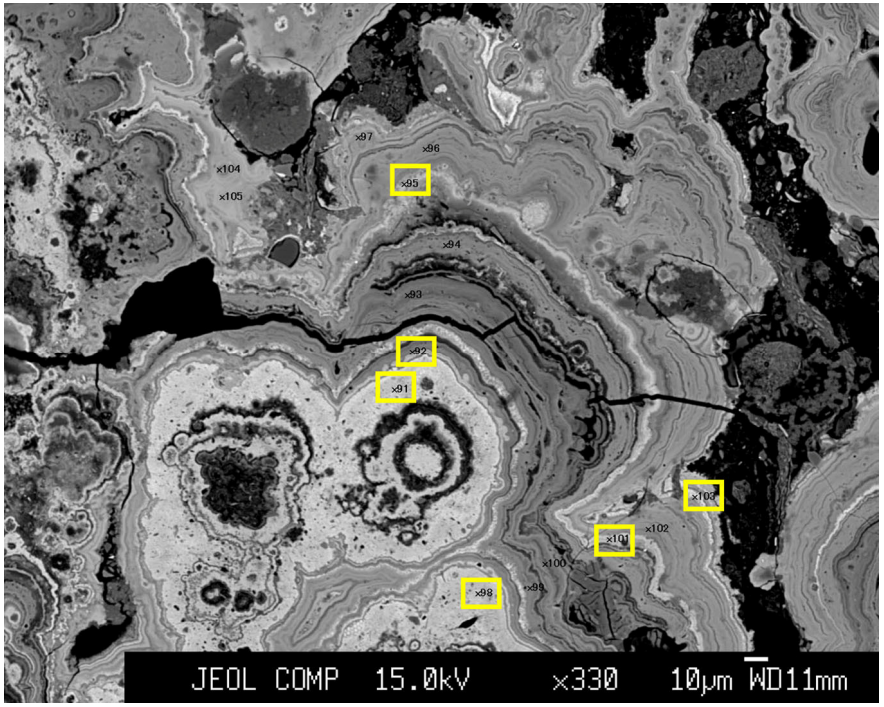

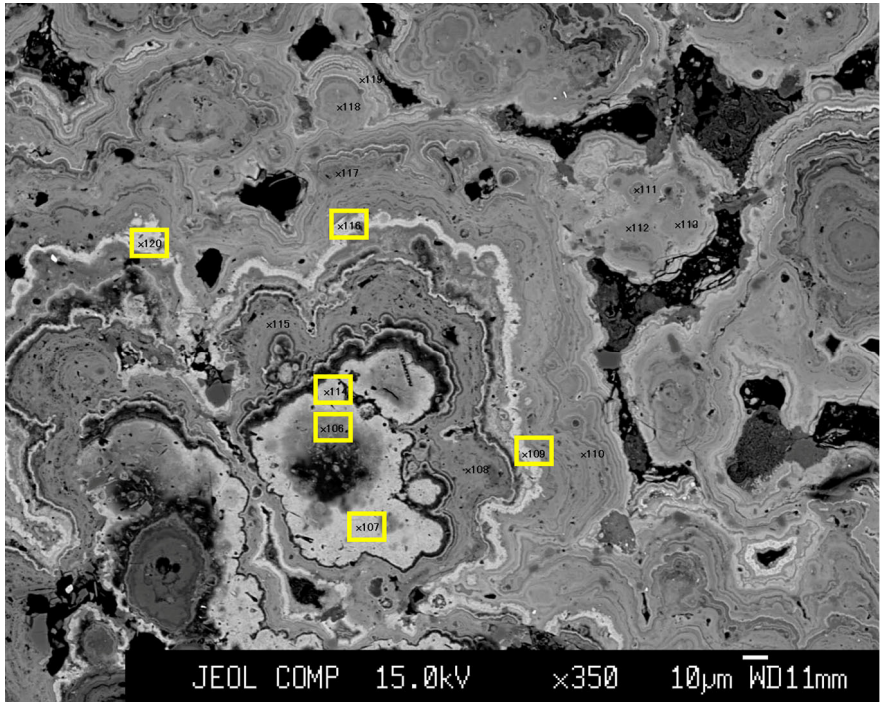

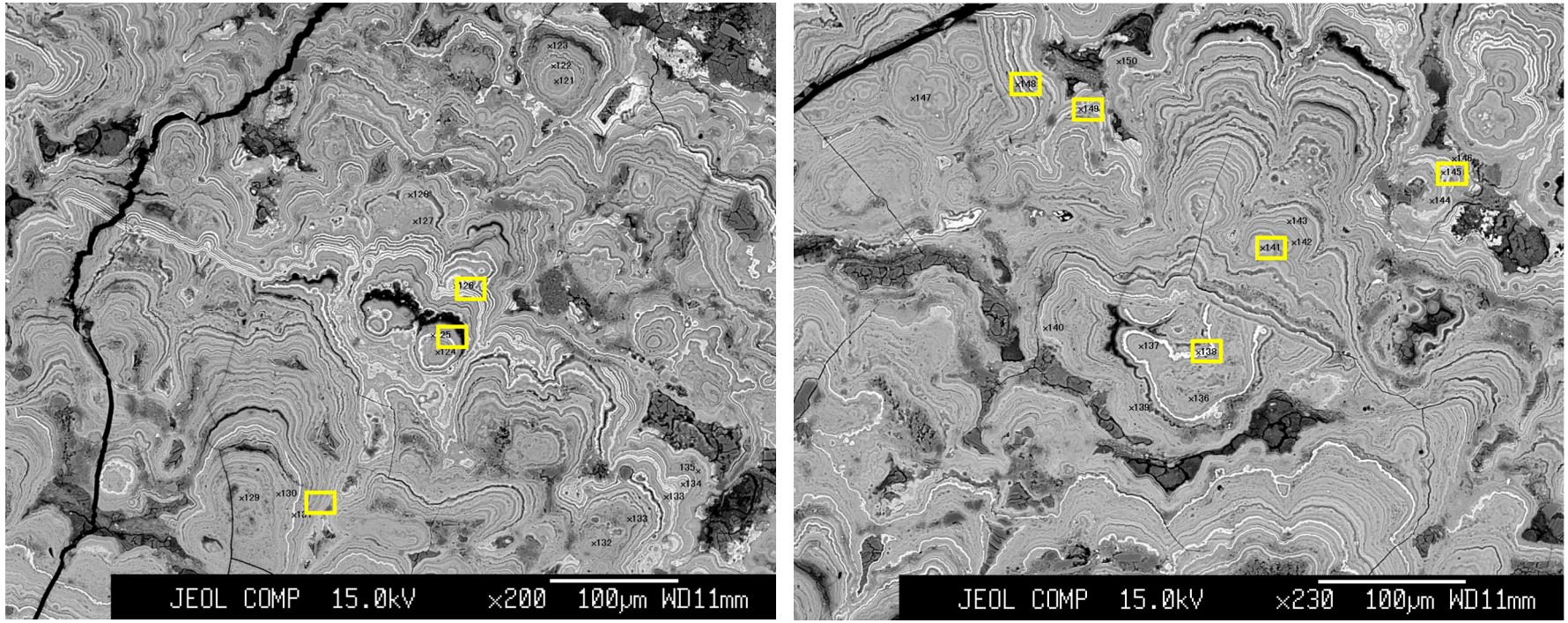

Figure S1. Surveys of the hydrogenetic-diagenetic growth discontinuity of the Fe-Mn nodule using backscattered electron images. This allows identification of Fe- and Mn-oxide phases that differ in brightness in the backscattered electron images. Black areas are voids, dark gray areas are clay phases, opaque gray areas are hydrogenetic regions, and bright gray areas are diagenetic regions. The analyzed spots are indicated with numbers and results are reported in Table S1 and the Supplementary material. The diagenetic spots are surrounded with yellow boxes. Image sizes are 360 (H) x 260 (V) μm^2 for the top two, and 530 (H) x 420 (V) μm^2 for the two below. Electron beam size is about 0.5-1.0 µm.

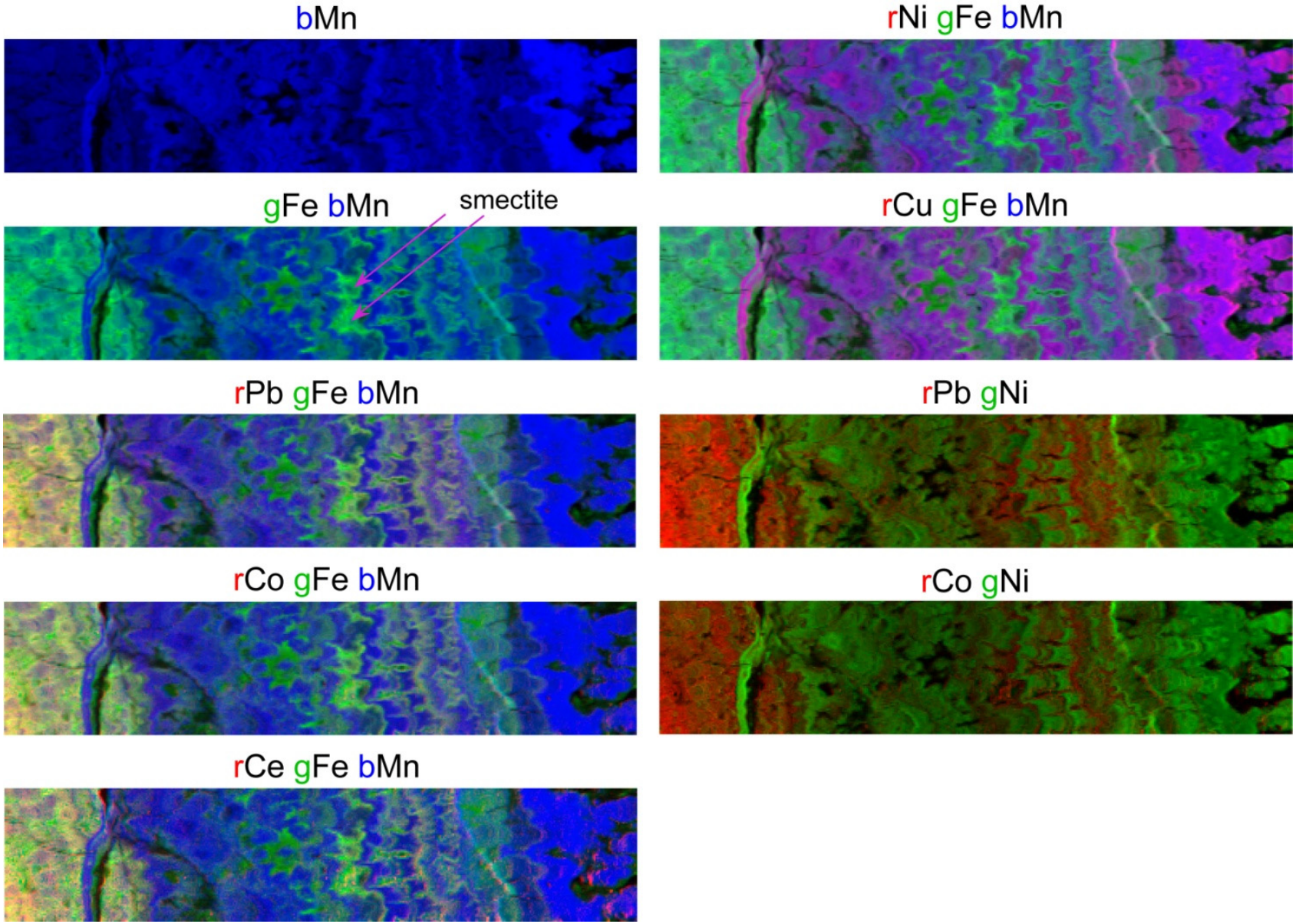

Figure S2. Synchrotron X-ray micro-fluorescence (SXRF) images of the distribution of trace metals and Fe and Mn in the hydrogenetic-diagenetic nodule (Map 3). The hydrogenetic region is to the left and the diagenetic region to the right. Two large smectite areas are indicated with arrows. Image size: 5910 (H) x 1250 (V) μm^2, pixel size: 15 (H) x 15 (V) μm^2.

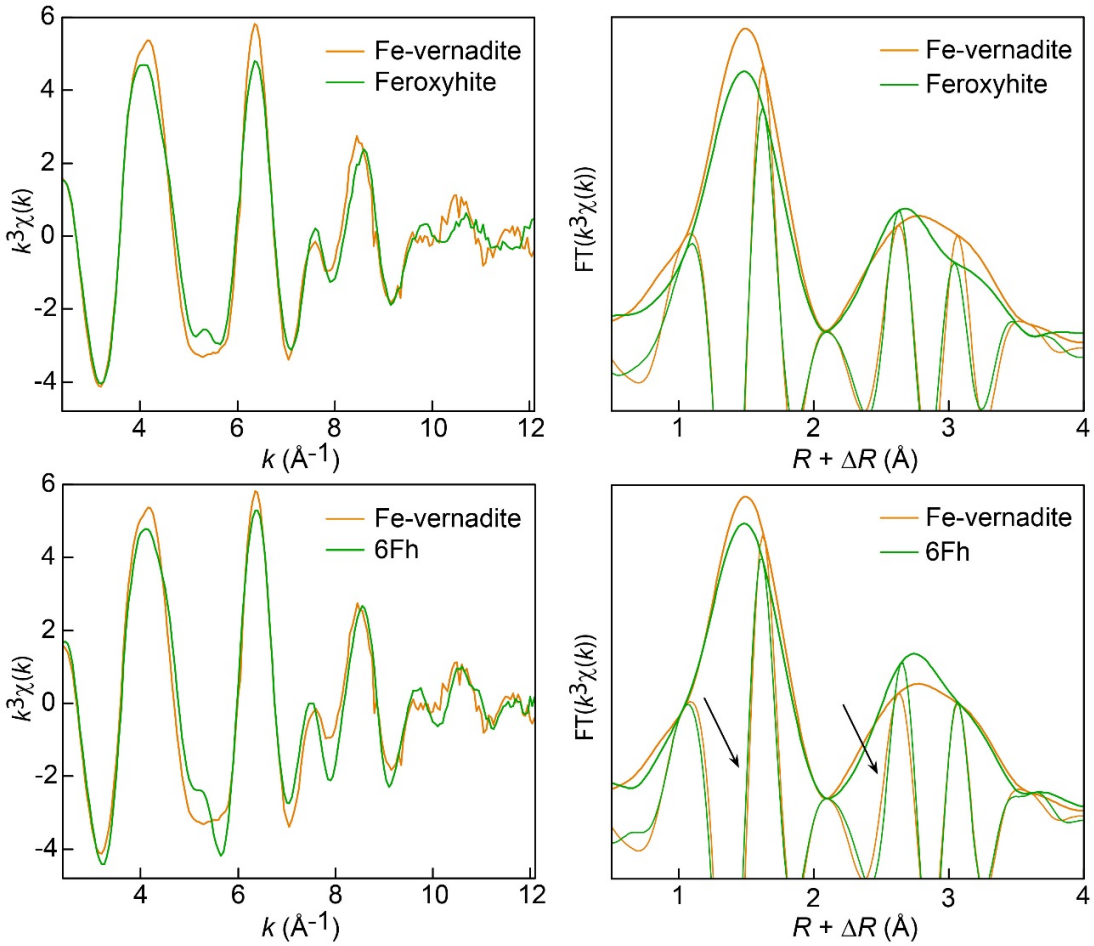

Figure S3. Fe K-edge EXAFS spectra and their Fourier transforms for Fe-vernadite and two models, feroxyhite (δ-FeOOH) and six-line ferrihydrite (6Fh). The magnitudes and imaginary parts of the Fourier transforms are shown. The small shifts in distance are more reliably detected by looking at the imaginary part than the magnitude. Arrows point out the phase difference in the Fourier transforms between the sample and 6Fh. The spectrum of Fe-vernadite is distinct from those of well-crystallized Fe oxyhydroxides (e.g., α- and β-FeOOH).

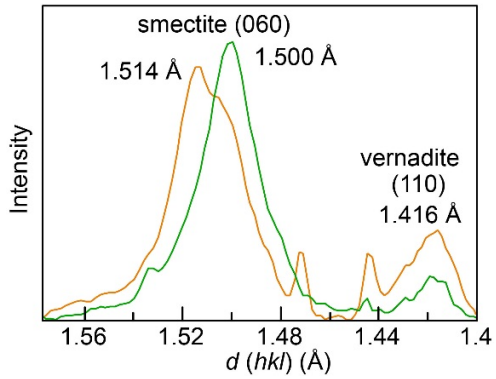

Figure S4. Two high-angle micro XRD patterns taken in clay-rich regions of the nodule showing the (060) reflection of the clay and the (110) reflection of vernadite. The 1.500 Å reflection identifies an aluminous smectite, and the 1.514 Å reflection an Fe-Al dioctahedral smectite.

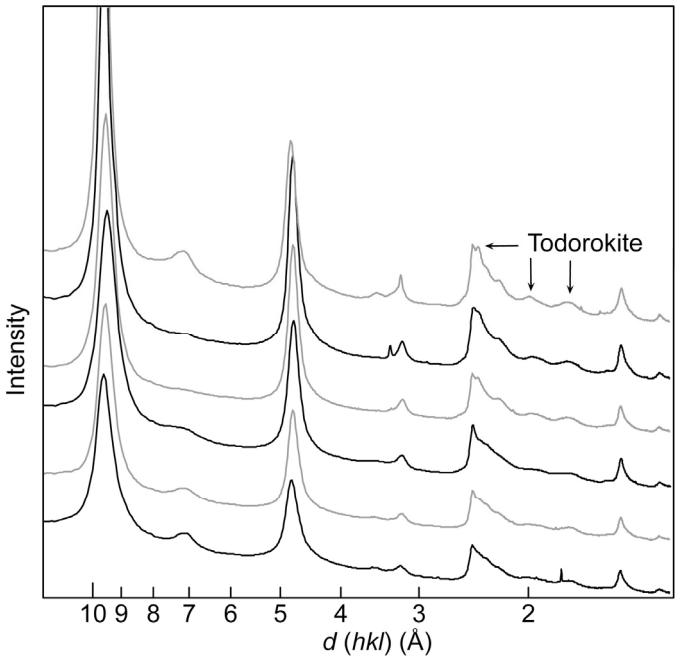

Figure S5. Micro-XRD patterns taken in the diagenetic nodule at different stages of the hydrogenetic to diagenetic transformation, as indicated by the increasing amount and crystallinity of todorokite. The simultaneous reinforcement of the basal reflection comes from the topotactic transition of 10Å-vernadite to todorokite (Bodei et al. 2007).

Figure S6 below is a compilation of XRD patterns from marine manganese oxides recorded at room condition and after in-situ vacuum dehydration. Some dehydrated samples were rehydrated in-situ in air at room temperature for several hours and a new pattern recorded.

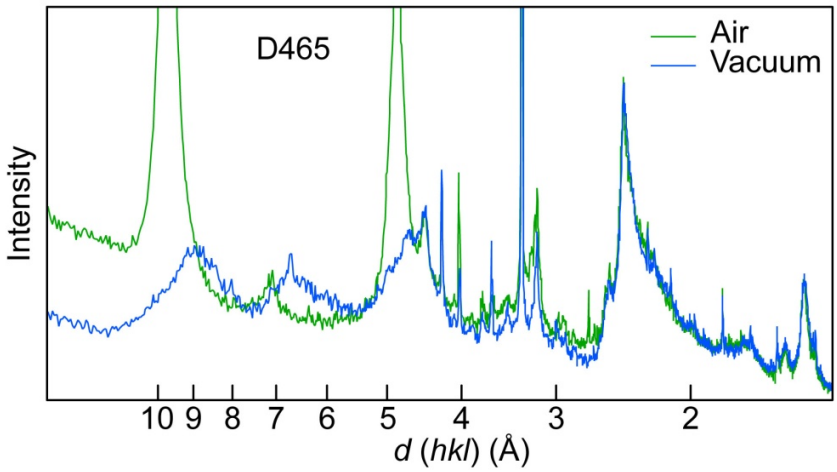

Figure S6a. XRD pattern of the D465 nodule in the hydrated and dehydrated state. Under vacuum, the composite (001) reflection from 10Å-vernadite splits into one reflection at ~8.9 Å from todorokite, and another at 6.5-7.0 Å from 7Å-vernadite (turbostratic birnessite). HRTEM imaging shows that 10Å-vernadite is a complex intergrowth of nano-sized domains of todorokite and vernadite (Bodei et al. 2007). The two types of crystallites are revealed upon dehydration.

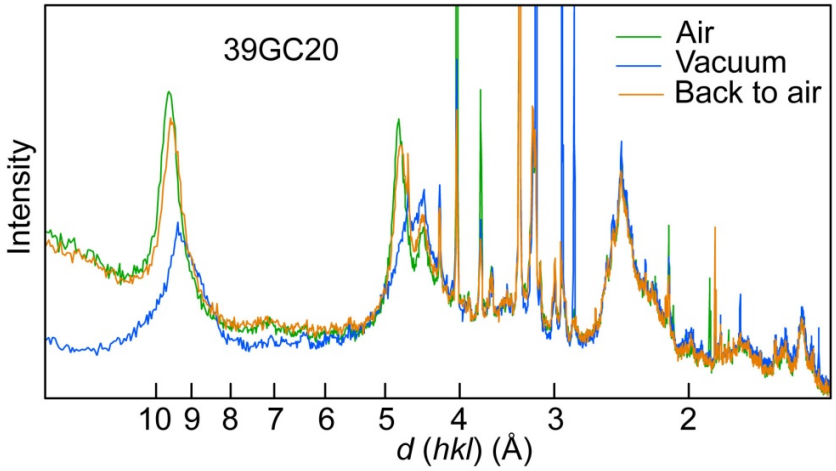

Figure 6b. XRD pattern of a manganese oxide (39GC20) collected near the 50GCC sample during the Ticoflux II cruise (2001) on the eastern flank of the East Pacific Rise (EPR) offshore Costa Rica (Courtesy of Dr. M. Buatier). The Mn oxide is almost pure todorokite. The narrow reflections are from quartz, anorthite and calcite.

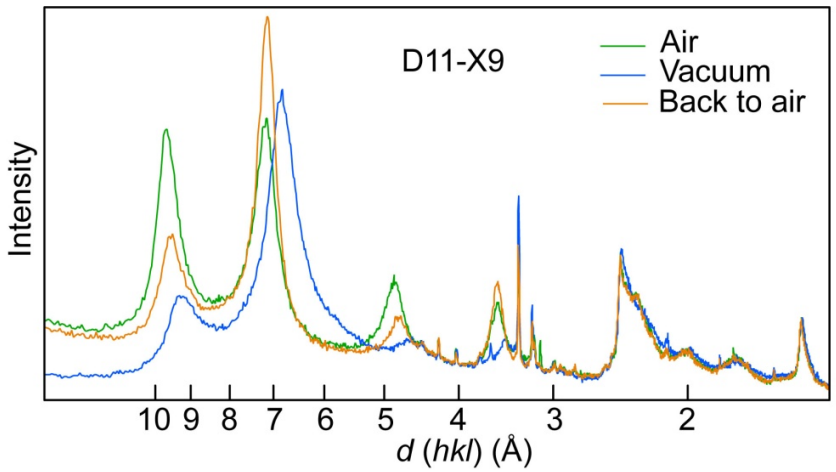

Figure S6c. XRD pattern of a manganese oxide (D11-X9) collected in an hydrothermal field in NW Pacific Ocean at 1575 m depth (Takahashi et al. 2007). Todorokite, 10Å-vernadite, and 7Å-vernadite comprise the majority of the sample. The weak reflection at 2.33 Å is from hexagonal birnessite, as shown below for sample D12-X2 collected in close proximity to D11-X9.

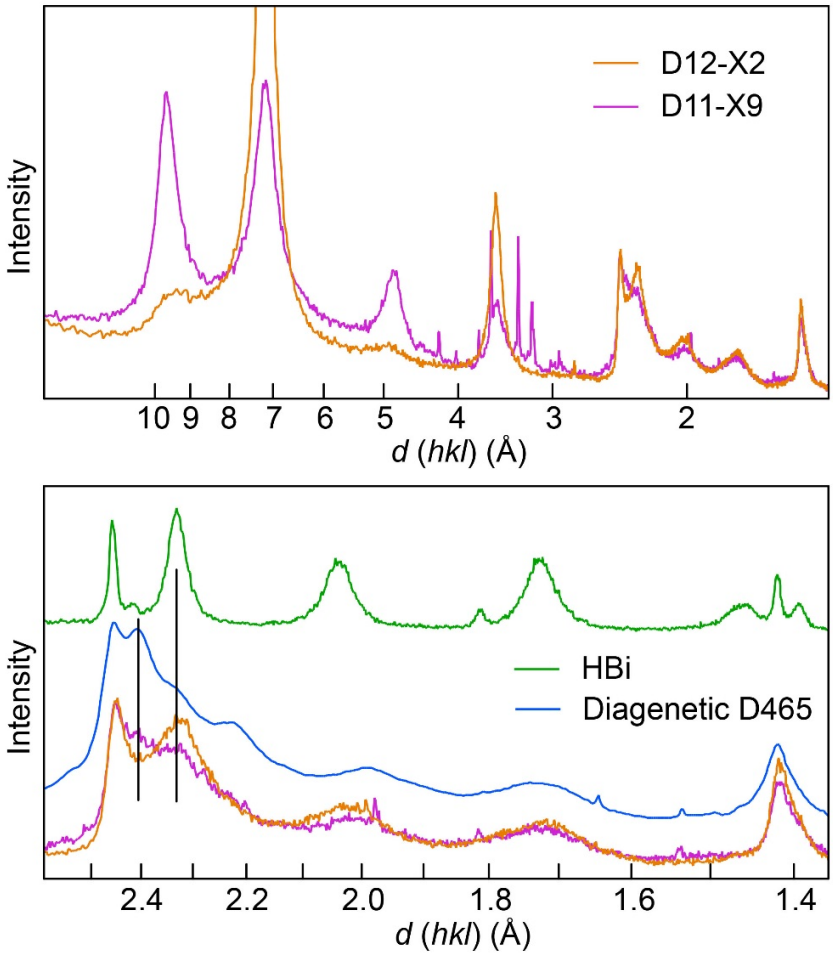

Figure S6d. XRD pattern of a manganese oxide (D12-X2), collected in the same hydrothermal field as D11-X9, compared to the patterns of D11-X9, synthetic hexagonal birnessite (Drits et al. 1997), and the micro-XRD pattern of 10Å-vernadite + todorokite shown in Figure 8a (diagenetic D465). The mineral composition of D12-X2 comprises todorokite, 10Å-vernadite, 7Å-vernadite, and hexagonal birnessite. The disordered 7Å-vernadite and ordered birnessite crystallites are probably interlayered (Lanson et al. 2000). All patterns were recorded in air.

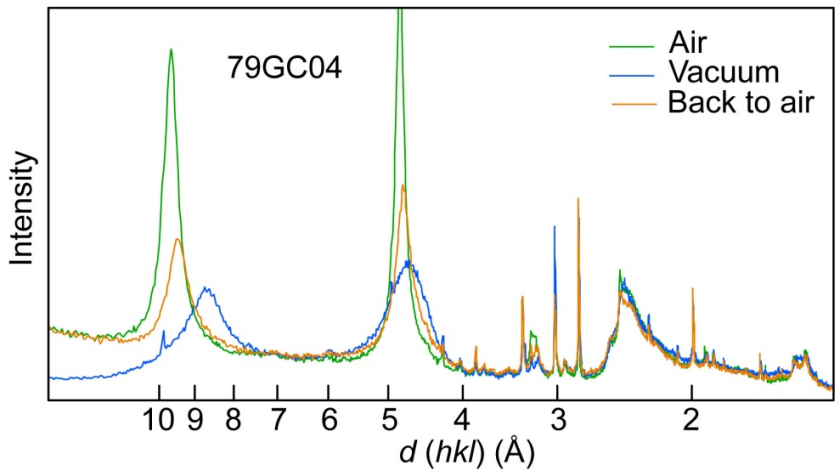

Figure S6e. XRD pattern of a manganese oxide (79GC04) collected in an hydrothermal field from the flank of the Juan de Fuca Ridge (Buatier et al. 2004). The Mn oxide is a turbostratic asbolane. This mixed-layer mineral is identified by the strong (002) reflection, which has a higher intensity than the (001) reflection, and a split of the two *hk*0 reflections. The intense (002) reflection indicates that the phyllomanganate interlayer contains an ordered layer from a metal (oxy)hydroxide, such as $Ni(OH)_2$, $Co(OH)_2$, $Cu(OH)_2$, or $Mn(OH)_2$ in the case of asbolane, or Al(OOH in the case of lithiophorite. The sub-lattices of the two interstratified layers are incommensurate in both the *a* and *b* directions, as indicated by the split of the (100) and (110) reflections (Chukhrov et al. 1980; Manceau et al. 1992).

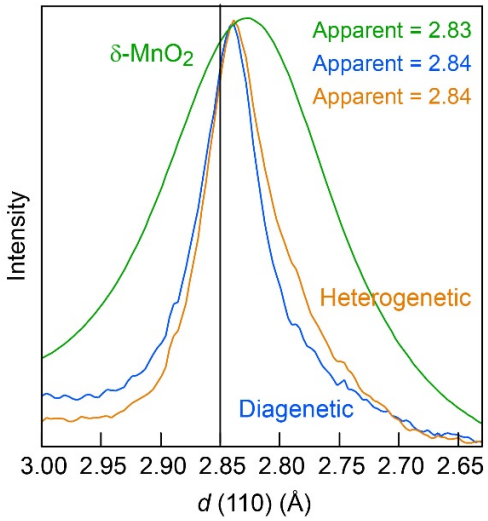

Figure S7. Profile of the (110) reflection of the nodule vernadite measured in the hydrogenetic and diagenetic regions (enlarged patterns from Fig. 8) compared to δ-MnO_2 equilibrated at pH 10 (Manceau et al. 2013). The three materials have a *b* value of 2.85 Å, but their peak maximum is shifted to lower 2x*d*(*hkl*) values in small particles to a greater extent the smaller the layer size.

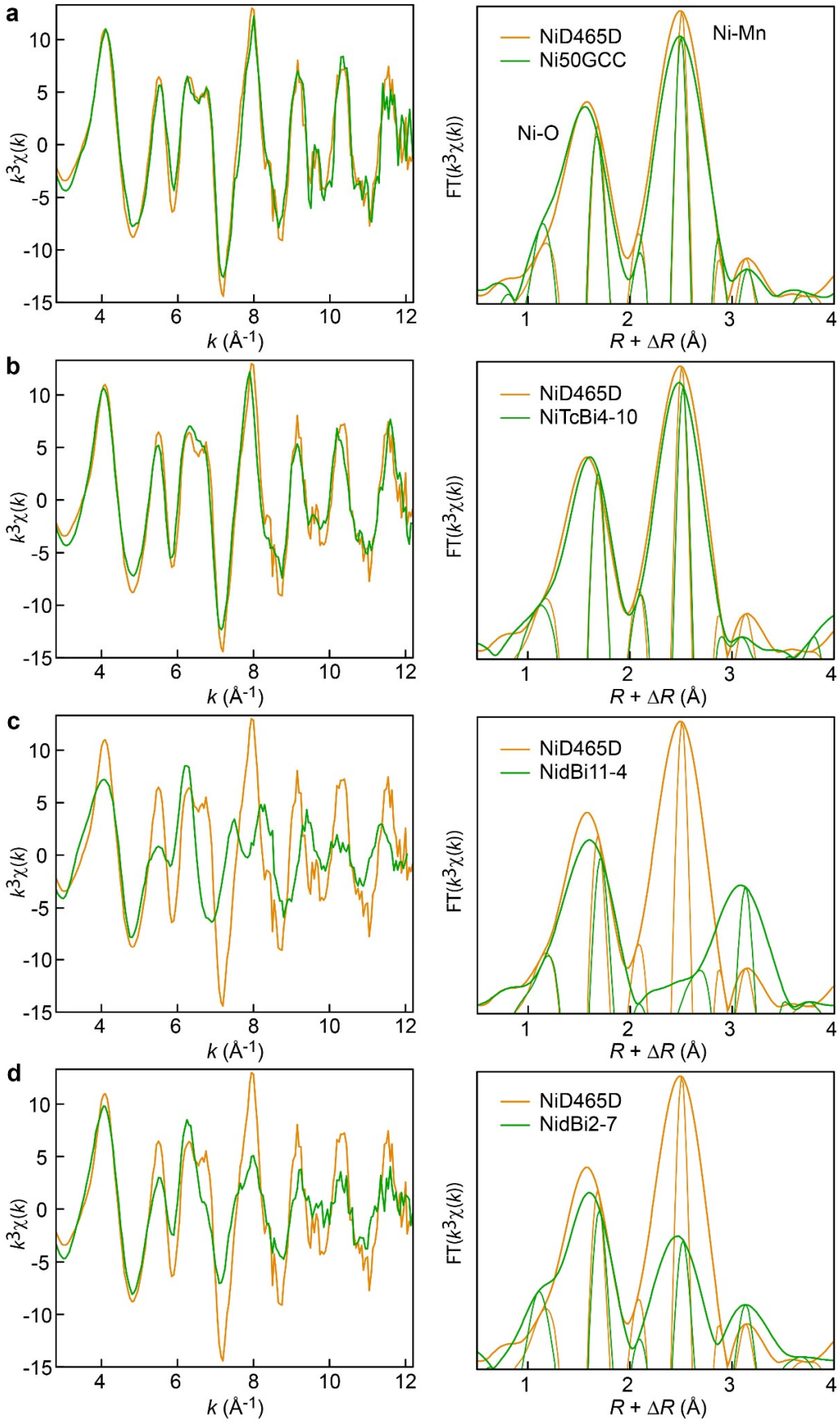
a
b
c
d
$k^3\chi(k)$
k (Å^{-1})
FT($k^3\chi(k)$)
$R + \Delta R$ (Å)
NiD465D
Ni50GCC
Ni-O
Ni-Mn
NiTcBi4-10
NidBi11-4
NidBi2-7

Figure S8. Ni K-edge EXAFS spectra and the magnitude and imaginary part of their Fourier transforms for the diagenetic nodule (NiD465D) and different models. (**a**) Mn deposit in hemipelagic sediments off Costa Rica from Bodei *et al.* (2007), in which Ni is partitioned among 10Å-vernadite and todorokite (Ni50GCC). (**b**) Ni incorporated in the MnO_2 layer of triclinic birnessite, similarly to Cu in CuTcBi7-10 (NiTcBi4-10). The Ni-O and Ni-Mn distances are a little longer in TcBi than in vernadite because TcBi has more Mn^{3+} (Manceau et al. 2005). (**c**,d) Ni-sorbed on δ-MnO_2 at pH 4 (Ni/Mn = 0.011; NidBi11-4) and pH 7 (Ni/Mn = 0.002 ; NidBi2-7) (Manceau et al. 2007). Ni is predominantly above vacancies in NidBi11-4 (TC complex, peak C), and occupies also layer vacancy sites in NidBi2-7 (peak B).

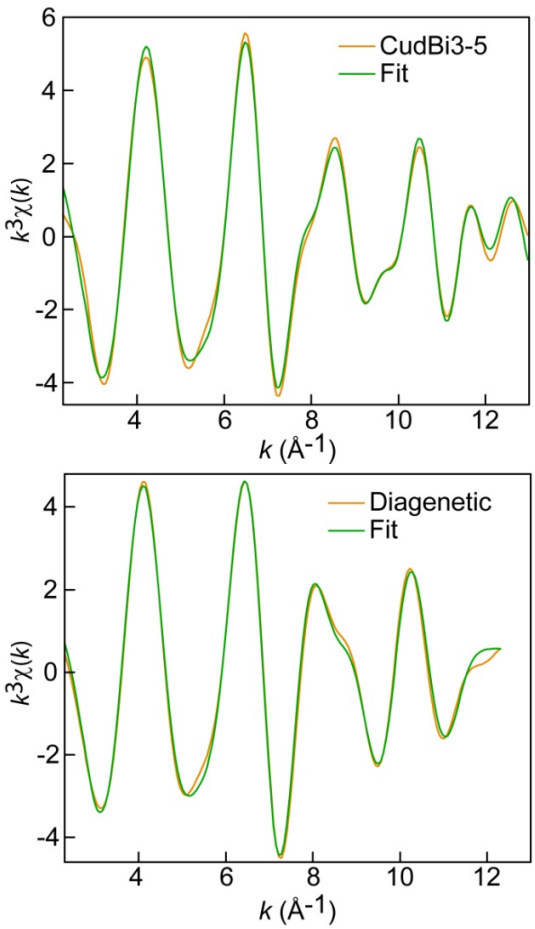

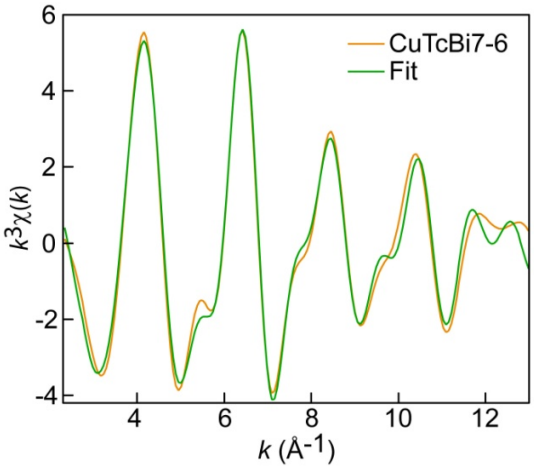

Figure S9. Multi-shell fit to Fourier-filtered Cu-O and Cu-Mn EXAFS data for CudBi3-5, CuTcBi7-6, and Cu in the diagenetic nodule D465. The fit parameters are listed in Table S2. The poorer simulation of CuTcBi7-6 comes from the omission in the fit of edge sites (DC complex) at about 3.68 Å. Although detected, their contribution is too weak to achieve stable solutions.

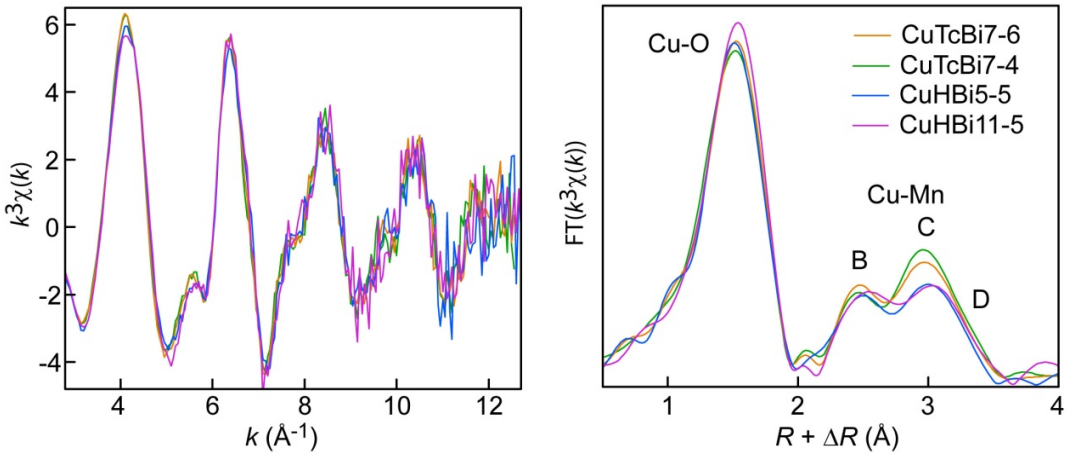

Figure S10. Cu K-edge EXAFS spectra and their Fourier transforms for Cu sorbed and incorporated in birnessite as a function of the equilibrium pH and sample preparation. Cu was coprecipitated with Mn in triclinic birnessite (TcBi) at pH 10 and the TcBi suspension subsequently equilibrated at pH 6 (CuTcBi7-6) or 4 (CuTcBi7-4). At acidic pH, TcBi is transformed to hexagonal birnessite (HBi). The two HBi samples were prepared by pre-equilibrating a TcBi suspension to pH 5 and the Cu sorbed at this pH directly on HBi. The synthesis route has little effect on the Cu partitioning among the layer site (E complex, peak B), interlayer site (TC complex, peak C), and edge site (DC complex, peak D). TcBi has a higher proportion of TC complex because its layers have a larger dimension.

Table S1. Mn/Fe ratios and trace metal concentrations (wt. %) shown in Figure 4 as measured by EPMA. The complete chemical analyses are given in the Supplementary material. The exact location of each analyzed spot is indicated on the backscattered electron images. The counting time was 40 s for the Ce and Pb fluorescence peaks and 2 x 20 s for the background counts measured on each side of the fluorescence peaks. These numbers are 20 s and 2 x 10 s for the other elements. The relative standard deviation (RSD) calculated from the total counts are 2% for Mg, Ca, Mn, and Fe, 6% for Ni and Cu, 20% for Na and Co, and 60% for Ce and Pb.

Spot #	Mn/Fe	Co	Ni	Cu	Ce	Pb	Mg	Ca	Na
91	160.87	0.121	3.096	2.127	0.022	-	3.912	1.466	0.286
92	9.51	0.121	2.262	1.428	0.000	-	2.729	1.815	0.214
93	1.60	0.350	0.255	0.259	0.098	0.109	0.491	2.651	0.111
94	1.23	0.313	0.157	0.217	0.120	0.061	0.534	2.266	0.030
95	27.51	0.263	2.728	1.946	0.000	0.012	4.780	1.181	0.038
96	1.41	0.278	0.218	0.248	0.060	0.008	0.685	2.457	0.075
97	1.31	0.175	0.587	0.495	0.054	0.107	1.222	2.374	0.066
98	71.33	0.092	3.084	2.211	0.051	0.019	3.023	1.681	0.297
99	2.26	0.143	0.721	0.555	0.072	0.045	0.906	2.003	0.294
100	1.84	0.238	0.348	0.316	0.071	0.089	0.677	2.492	0.238
101	13.36	0.170	2.629	2.040	0.019	0.014	4.779	1.067	0.160
102	1.60	0.252	0.280	0.336	0.076	0.082	0.752	2.562	0.146
103	5.86	0.296	2.221	1.380	0.031	0.023	2.415	1.842	0.154
104	1.27	0.200	0.273	0.304	0.089	0.074	0.885	2.749	0.096
105	0.95	0.190	0.207	0.348	0.078	0.064	0.841	2.699	0.091
106	30.16	0.020	2.508	1.596	0.016	0.001	3.691	1.303	0.079
107	216.50	0.027	3.550	2.104	0.017	0.066	4.186	1.274	0.133
108	1.41	0.339	0.274	0.275	0.103	0.036	0.650	2.570	0.098
109	47.15	0.082	3.535	1.828	0.000	0.007	3.726	1.241	0.135
110	1.57	0.212	0.259	0.323	0.078	0.055	0.695	2.464	0.126

111	1.55	0.207	0.430	0.409	0.081	0.035	0.921	2.243	0.102
112	1.00	0.182	0.146	0.252	0.129	0.072	0.706	2.379	0.151
113	1.16	0.215	0.141	0.233	0.103	0.092	0.725	2.401	0.189
114	56.68	0.001	3.116	2.061	0.025	-	5.065	1.260	0.131
115	1.61	0.315	0.284	0.284	0.115	0.113	0.666	2.722	0.058
116	24.86	0.114	3.133	1.775	0.033	0.024	3.522	1.362	0.263
117	1.67	0.274	0.305	0.235	0.061	0.046	0.592	2.330	0.148
118	1.42	0.222	0.427	0.479	0.094	0.080	1.075	2.492	0.029
119	2.17	0.222	1.268	0.930	0.054	0.053	1.705	1.929	0.013
120	102.00	0.082	3.693	1.780	0.014	-	3.717	1.304	0.206
121	3.44	0.271	0.868	0.960	0.037	0.103	0.444	2.274	0.177
122	3.53	0.273	1.299	1.569	0.058	0.056	0.785	2.011	0.109
123	3.40	0.247	1.130	1.344	0.026	0.023	0.782	1.922	0.175
124	2.61	0.291	0.620	0.745	0.079	0.053	0.418	2.408	0.185
125	14.51	0.060	2.866	2.719	0.103	0.019	4.199	1.286	0.217
126	16.30	0.172	2.824	2.828	0.017	0.063	4.125	1.318	0.199
127	3.10	0.301	0.875	0.906	0.044	0.037	1.202	2.489	0.226
128	3.71	0.200	1.073	1.149	0.108	0.058	1.597	2.441	0.206
129	2.81	0.306	0.517	0.581	0.090	0.048	0.883	1.728	0.146
130	2.57	0.384	0.451	0.547	0.120	0.106	1.103	2.449	0.208
131	4.13	0.279	1.781	1.702	0.040	0.053	3.055	1.759	0.177
132	2.03	0.356	0.469	0.598	0.120	0.071	0.881	2.239	0.082
133	1.88	0.274	0.290	0.423	0.072	0.050	0.732	2.344	0.277
134	2.17	0.243	0.570	0.749	0.113	0.052	1.068	2.610	0.226
135	4.61	0.169	2.034	1.960	0.013	0.046	3.266	1.765	0.260
136	2.82	0.374	0.604	0.691	0.064	0.126	1.105	2.375	0.122
137	2.98	0.362	0.720	0.744	0.107	0.050	1.062	2.456	0.226
138	5.03	0.253	1.994	1.448	0.077	0.087	2.139	1.918	0.115
139	1.41	0.222	0.211	0.427	0.138	0.051	0.820	2.150	0.224
140	1.82	0.305	0.331	0.507	0.104	0.034	0.846	2.259	0.201
141	6.73	0.282	1.796	1.920	0.072	0.033	2.268	1.894	0.188
142	2.55	0.313	0.504	0.603	0.135	0.074	0.854	2.352	0.085
143	3.02	0.291	0.627	0.745	0.104	0.028	0.930	2.252	0.174
144	1.66	0.220	0.481	0.664	0.090	0.053	1.126	2.258	0.131
145	5.27	0.198	2.045	2.077	0.023	0.033	3.254	1.685	0.287
146	1.27	0.196	0.299	0.508	0.081	0.069	0.768	2.164	0.182
147	2.79	0.404	0.622	0.698	0.106	0.069	0.860	2.474	0.054
148	4.04	0.158	1.743	1.709	0.041	0.078	2.820	1.733	0.148
149	5.19	0.182	1.968	2.045	0.010	0.039	3.084	2.253	0.168
150	1.52	0.211	0.321	0.582	0.132	0.065	0.896	2.206	0.093

Table S2. EXAFS parameters from multi-shell fits of Cu-EXAFS data

	Cu-O			Cu-Mn		Cu-Mn		Cu-Mn				
	CN	*R*(Å)	σ(Å^2)	*CN*	*R*(Å)	*CN*	*R*(Å)	*CN*	*R*(Å)	σ(Å^2)	Δ*E*	*Res*
CudBi3-5	4.6	1.94	0.007	0.8	2.87*	1.3	3.40*	0.6	3.68	0.005†	-0.4	9.6
CuTcBi7-6	4.7	1.96	0.007	0.8	2.86	2.3	3.40			0.007†	-2.0	14.1
Diagenetic	4.1	1.96	0.006	1.6	2.88					0.008	-1.6	7.6

Notes: CN is the effective number of atomic pairs seen by EXAFS, *R* is the interatomic distance, σ is the standard deviation of the distance distribution, Δ*E* is the threshold energy correction in eV, and *Res* is the fit residual defined as $[\Sigma\{|\chi_{exp} - \chi_{fit}|\}/\Sigma\{|\chi_{exp}|\}] \times 100$. The many body amplitude-reduction factor S_0^2 was fixed to 0.9.
* fixed values.
† Constrained to the same value for all Cu-Mn pairs.

References cited

Bodei, S., Manceau, A., Geoffroy, N., Baronnet, A., and Buatier, M. (2007) Formation of todorokite from vernadite in Ni-rich hemipelagic sediments. Geochimica et Cosmochimica Acta, 71, 5698–5716.

Buatier, M.D., Guillaume, D., Wheat, C.G., Hervé, L., and Adatte, T. (2004) Mineralogical characterization and genesis of hydrothermal Mn oxides from the flank of the Juan the Fuca Ridge. American Mineralogist, 89, 1807-1815.

Chukhrov, F.V., Gorshkov, A.I., Vitovskaya, I.V., Drits, V.A., Sivtsov, A.V., and Rudnitskaya, E.S. (1980) Crystallochemical nature of Co-Ni asbolan. Izvestia Akademia Nauk, SSSR, Seriya Geologicheskaya, 6, 73-81. (Translated in International Geological Review 24, 598-604, 1982).

Drits, V.A., Silvester, E., Gorshkov, A.I., and Manceau, A. (1997) The structure of synthetic monoclinic Na-rich birnessite and hexagonal birnessite. Part 1. Results from X-ray diffraction and selected area electron diffraction. American Mineralogist, 82, 946-961.

Lanson, B., Drits, V.A., Silvester, E.J., and Manceau, A. (2000) Structure of H-exchanged hexagonal birnessite and its mechanism of formation from Na-rich monoclinic buserite at low pH: New data from X-ray diffraction. American Mineralogist, 85, 826-835.

Manceau, A., Gorshkov, A.I., and Drits, V.A. (1992) Structural chemistry of Mn, Fe, Co, and Ni in Mn hydrous oxides. II. Information from EXAFS spectroscopy, electron and X-ray diffraction. American Mineralogist, 77, 1144-1157.

Manceau, A., Lanson, M., and Geoffroy, N. (2007) Natural speciation of Ni, Zn, Ba and As in ferromanganese coatings on quartz using X-ray fluorescence, absorption, and diffraction. Geochimica Cosmochimica Acta, 71, 95-128.

Manceau, A., Marcus, M.A., Grangeon, S., Lanson, M., Lanson, B., Gaillot, A.C., Skanthakumar, S., and Soderholm, L. (2013) Short-range and long-range order of phyllomanganate nanoparticles determined using high energy X-ray scattering. Journal of Applied Crystallography, 46, 193-209.

Manceau, A., Tommaseo, C., Rihs, S., Geoffroy, N., Chateigner, D., Schlegel, M., Tisserand, D., Marcus, M.A., Tamura, N., and Chen, Z.S. (2005) Natural speciation of Mn, Ni and Zn at the micrometer scale in a clayey paddy soil using X-ray fluorescence, absorption, and diffraction. Geochimica et Cosmochimica Acta, 69, 4007-4034.

Takahashi, Y., Manceau, A., Geoffroy, N., Marcus, M.A., and Usui, A. (2007) Chemical and structural control of the partitioning of Co, Ce, and Pb in marine ferromanganese oxides. Geochimica et Cosmochimica Acta, 71, 984-1008.